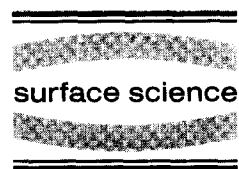




ELSEVIER

Surface Science 355 (1996) 229–240



Spinodal decomposition and pattern formation near a crystalline surface

Chengwei Geng, Long-Qing Chen *

Department of Materials Science and Engineering, The Pennsylvania State University, University Park, PA 16802, USA

Received 15 June 1995; accepted for publication 25 October 1995

Abstract

The kinetics of spinodal decomposition and morphological evolution near a crystalline surface (an edge in two dimensions) were investigated by microscopic master equations in both the point and pair approximations and a second-neighbor interaction model in a two-dimensional model system. It is shown that, in the presence of a surface, spinodal decomposition initially involves surface segregation, followed by anisotropic decomposition in the near-surface region, with subsequent isotropic decomposition in the bulk. It is demonstrated that, due to segregation, a surface spinodal decomposition may take place for alloys whose overall average compositions are outside the bulk spinodal. It is found that the presence of a surface results in a dominant concentration wave, which produces interesting transient morphological patterns such as distorted hexagonal precipitate lattices for relatively low-volume fractions and straight stripes at high-volume fractions in the near-surface region. The effect of pair correlations on the kinetics of spinodal decomposition and morphologies was studied.

Keywords: Computer simulations; Low index single crystal surfaces; Models of non-equilibrium phenomena; Non-equilibrium thermodynamics and statistical mechanics; Surface segregation; Surface thermodynamics

1. Introduction

The kinetics of spinodal decomposition and accompanying morphological evolution are well understood in bulk crystalline solids. In the absence of elastic stress and interfacial energy anisotropy, spinodal decomposition is manifested by the growth of concentration waves with wave numbers around zero, resulting in an isotropic interconnected morphology for the critical ($c = 0.5$, or close to critical) composition and spherical second-phase particles embedded in a matrix for off-critical compositions. However, this is a correct

picture only for bulk systems in which the effect of surfaces due to finite size can be ignored. As the size of a system decreases, for example, down to the nanoscale, as in nano-crystalline particles and nanoscale or atomic-scale thin films, it is expected that the surface becomes increasingly important in both the structural and phase transformation behaviors. Thermodynamically, the contribution from the surface and interfacial energy to the total free energy in such systems may become comparable to the bulk free energy and hence, cannot be ignored. As a result, the phase stability and phase diagram of a nanoscale system could be dramatically different from the corresponding macroscopic ones [1]. Kinetically, the presence of a surface results in a difference in the growth of concen-

* Corresponding author. Fax: +1 814 865 0016; e-mail: chen@ems.psu.edu.

tration waves perpendicular and parallel to the surface due to the breaking of translational symmetries perpendicular to the surface. Therefore, it is expected that the morphological pattern formation will be quite different near a free surface from that in the bulk. Depending on the relative size of particles or thickness of thin films to the typical spinodal wavelength, the two-phase morphology of a nanoscale particle or thin film can be dominated by the presence of a surface. Indeed, it was found experimentally that the presence of a free surface led to the development of a dominant concentration wave with the wave vector perpendicular to the surface during spinodal decomposition of a polymer film [2].

There have been many theoretical investigations and numerical simulations of surface segregation and phase transitions near a surface in the last two decades [3–12]. Most of the recent works on the kinetics of spinodal decomposition near a surface employed the continuum Cahn–Hilliard-type of equations [9–12]. Microscopic kinetic models of the thermodynamics of surface segregation and phase transitions in the surface region usually treat a system with a surface inhomogeneous only perpendicular to the surface [7,8]. By including a free energy contribution from the surface in the Cahn–Hilliard equation, the dominant concentration wave perpendicular to the surface as observed experimentally was predicted in a number of numerical simulations [9–12]. Morphologically, the presence of a surface results in a morphology with long stripes parallel to the surface during spinodal decomposition.

In this paper, we apply a microscopic model, the cluster activation method [13], derived from microscopic master equations [14]. We do not make the assumption that atom flux is linearly proportional to the thermodynamic driving force, as in the Cahn–Hilliard equation [15]. Therefore, it can be applied to highly non-equilibrium processes which take place in systems far from equilibrium. The free energy function does not explicitly enter the kinetic equations. Due to the microscopic nature of the model, it can be applied to both ordering and spinodal decomposition with a surface. Moreover, in this model, the structural state of a system is described by multiparticle-distribu-

tion functions or cluster probabilities. As a result, the effect of high order correlations on the kinetics of spinodal decomposition can be studied. At the same level of approximation, the equilibrium states derived from the cluster activation method correspond to those calculated by the equilibrium cluster variation method [16] which is being widely used in the equilibrium phase diagram calculations.

Although, in principle, Monte Carlo may be applied to the same problem studied in this paper, there are a number of reasons why we chose the kinetic equation approach instead of Monte Carlo. First of all, the probability distribution functions generated by the kinetic equations are averages over a time-dependent non-equilibrium ensemble, whereas in Monte Carlo a series of snapshots of instantaneous atomic configurations along the simulated Markov chain are produced. Therefore, a certain averaging procedure has to be designed in the Monte Carlo technique in order to obtain the information about local composition or local order. Secondly, while the time scale is clearly defined in the microscopic master equations, it is rather difficult to relate the Monte Carlo time steps to real time. Finally, in most cases simulations based on kinetic equations are computationally more efficient than Monte Carlo. This is also the main reason that most of the equilibrium phase diagram calculations in alloys were performed using the cluster variation method instead of Monte Carlo. The main disadvantage of the microscopic kinetic equations is the fact that equations become increasingly tedious when increasingly higher order correlations are included, whereas in Monte Carlo essentially all correlations are automatically included.

The main purpose of this work is to study the kinetics of spinodal decomposition as well as the morphologies near a crystalline surface at various conditions. For this purpose, we employed a two-dimensional square lattice with a second-neighbor interaction model, and in this case a surface is in fact an edge. A free surface is treated as a simple termination of a bulk crystal and the effect of lattice relaxation is not considered. As will be shown below, the presence of a surface results in a wide variety of interesting spinodal morphologies, some of which have not been predicted previously.

The effect of pair correlations, composition, as well as the bond energies between atoms on the spinodal decomposition kinetics and morphologies will be discussed.

2. The model

2.1. Probability distribution functions

In general, the structural state of an alloy with two kinds of atoms A and B can be described by a set of multiparticle distribution functions, $P_{a_1, \dots, a_n}(\mathbf{r}_1, \dots, \mathbf{r}_n, t)$, which are the joint probabilities of atoms, a_1, \dots, a_n ($a = A$ or B), occupying lattice positions $\mathbf{r}_1, \dots, \mathbf{r}_n$ simultaneously at time t . A complete description of a structural state requires the knowledge of all the distribution functions. For a binary system with N lattices, the number of independent distribution functions is $2^N - 1$ which is a huge number for any practical system. In practice, therefore, we have to resort to approximations in order to make the number of distribution functions tractable. The simplest approximation is, of course, the single-site point approximation in which the structural state is described by the single-site occupation probabilities, $P_A(\mathbf{r})$ or $P_B(\mathbf{r})$. A single-site approximation together with a first-neighbor interaction model is exactly the classical Bragg–William model in the thermodynamics of solid solutions. The next level of approximation is the pair approximation in which the structural state of an alloy is described by the point and pair distribution functions. The thermodynamic model employing a pair approximation and a nearest-neighbor interaction model corresponds to the Bethe approximation. As we move to higher level approximations, the formulation becomes increasingly tedious and complicated as the number of distribution functions increases exponentially. In the current work, we employ both point and pair approximations, and with both first- and second-neighbor pairwise interactions.

A consistent description of a thermodynamic state requires that all the distribution functions satisfy the normalization condition. In the pair approximation, the normalization conditions for

$P_\alpha(\mathbf{r})$ and $P_{\alpha_1, \alpha_2}(\mathbf{r}_1, \mathbf{r}_2)$ are given by

$$\begin{aligned} \sum_{\alpha} P_{\alpha}(\mathbf{r}) &= 1, \\ \sum_{\alpha_2} P_{\alpha_1, \alpha_2}(\mathbf{r}_1, \mathbf{r}_2) &= P_{\alpha_1}(\mathbf{r}_1), \\ \sum_{\alpha_1} P_{\alpha_1, \alpha_2}(\mathbf{r}_1, \mathbf{r}_2) &= P_{\alpha_2}(\mathbf{r}_2). \end{aligned} \quad (1)$$

Therefore, the distribution functions are not independent. Among them, we can choose an independent set, e.g., $P_A(\mathbf{r})$ and $P_{AA}(\mathbf{r}_1, \mathbf{r}_2)$. All other points and pair variables may be obtained from this independent set according to the normalization condition (1).

2.2. Kinetic equations

Since our main interest is in the kinetics of phase transformations in general and spinodal decomposition in particular near a surface, all the distribution functions are time-dependent, evolving from values corresponding to non-equilibrium states towards equilibrium. To describe the change of distribution functions as a function of time and therefore the kinetics of spinodal decomposition, we have to assume an atomic diffusion mechanism. In this paper, we assume the simple direct exchange mechanism although the vacancy mechanism is more realistic for alloy systems and although the vacancy mechanism can be treated in this model [14,17]. As we employ a second-neighbor interaction model, the relevant distribution functions are point, first-neighbor pair and second-neighbor pair distribution functions which completely characterize the structural states in the pair approximation. We also assume an isothermal environment although the model can easily deal with non-isothermal cases. Because of the normalization conditions, we only need to solve the kinetic equations describing the independent distribution functions.

To write down the kinetic equations, we consider a pair of exchange sites at \mathbf{r} and a nearest-neighbor site, $\mathbf{r} + \delta$, and a set $\{x\}$ of nearby influence sites which can affect the exchange reaction. If we have an A atom at \mathbf{r} , a B atom at $\mathbf{r} + \delta$, and a set of atoms $\{X\}$ at $\{x\}$, we use $R_{AB}(\{X\})$ to represent the rate at which the AB pair exchanges under the

influence of the set of neighboring atoms $\{X\}$. Similarly, $R_{BA}(\{X\})$ is the rate at which a BA pair will exchange under the same environment when a B atom is at r , and an A atom is at $r + \delta$. Then the rates of change of $P_A(r)$ and $P_{AA}(r_1, r_2)$ are given by

$$\frac{dP_A(r)}{dt} = \sum_{\delta} \sum_{\{X\}} P_{BA\{X\}}(r, r + \delta, \{X\}) R_{BA}(\{X\}) - \sum_{\delta} \sum_{\{X\}} P_{AB\{X\}}(r, r + \delta, \{X\}) R_{AB}(\{X\}), \quad (2)$$

$$\begin{aligned} \frac{dP_{AA}(r_1, r_2)}{dt} = & \sum_{\delta \neq r_1 - r_2} \sum_{\{X\}} P_{ABA\{X\}} \\ & \times (r_1, r_2, r_2 + \delta, \{X\}) R_{BA}(\{X\}) \\ & + \sum_{\delta \neq r_2 - r_1} \sum_{\{X\}} P_{BAA\{X\}} \\ & \times (r_1, r_2, r_1 + \delta, \{X\}) R_{BA}(\{X\}) \\ & - \sum_{\delta \neq r_1 - r_2} \sum_{\{X\}} P_{AAB\{X\}} \\ & \times (r_1, r_2, r_2 + \delta, \{X\}) R_{AB}(\{X\}) \\ & - \sum_{\delta \neq r_2 - r_1} \sum_{\{X\}} P_{AAB\{X\}} \\ & \times (r_1, r_2, r_1 + \delta, \{X\}) R_{AB}(\{X\}), \quad (3) \end{aligned}$$

where Σ_{δ} denotes the summation over all the nearest-neighbor sites, $r + \delta$, of r . In Eqs. (2) and (3), $P_{\alpha_1, \alpha_2, \dots, \alpha_n}(r_1, r_2, \dots, r_n)$ represents the joint probability of $\alpha_1, \alpha_2, \dots, \alpha_n$ occupying r_1, r_2, \dots, r_n simultaneously. For example, $P_{AB\{X\}}(r, r + \delta, \{X\})$ is the probability of finding an A atom at r , a B atom at $r + \delta$, and the set $\{X\}$ of atoms at the neighboring sites $\{x\}$ simultaneously.

2.3. Superposition approximation

In order to carry out the summations in the right-hand side of Eqs. (2) and (3), we need to express the joint probability distributions, $P_{AB\{X\}}(r, r + \delta, \{X\})$, etc., in terms of independent point and pair distribution functions. For this purpose, we invoke the superposition approximation. To briefly explain the superposition approximation, let us take a look at a three-point cluster (Fig. 1). If the only known information is the point and nearest-neighbor pair distribution functions, we can approximate the triplet distribution func-

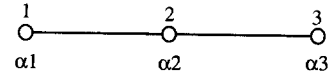


Fig. 1. A 3-point linear cluster.

tion by

$$P_{\alpha_1, \alpha_2, \alpha_3}(1, 2, 3) = P_{\alpha_1, \alpha_2}(1, 2) \times P_{\alpha_2, \alpha_3}(2, 3) / P_{\alpha_2}(2).$$

Therefore, in the first- and second-neighbor pair approximation of a square lattice,

$$\begin{aligned} P_{AB\{X\}}(r, r + \delta, \{X\}) = & [P_{AB}(r, r + \delta) P_{X_1A}(x_1, r) P_{AX_3}(r, x_3) P_{BX_4}(r + \delta, x_4) \\ & \times P_{BX_6}(r + \delta, x_6) P_{X_8B}(x_8, r + \delta) P_{X_9A}(x_9, r) \\ & \times P_{AX_2}(r, x_2) P_{AX_4}(r, x_4) P_{BX_3}(r + \delta, x_3) \\ & \times P_{BX_5}(r + \delta, x_5) P_{X_7B}(x_7, r + \delta) P_{X_8A}(x_8, r) \\ & \times P_{X_9B}(x_9, r + \delta) P_{X_{10}A}(x_{10}, r)] \\ & \times [(P_A(r))^7 (P_B(r + \delta))^7]^{-1}, \quad (4) \end{aligned}$$

where $x_1 \dots x_{10}$ are the individual sites in the set of neighboring sites around the A–B pair at r and $r + \delta$, and X_1, \dots, X_{10} are the types of atoms occupying those sites as shown in Fig. 2. In Eq. (4), the correlations for the pairs which are not directly connected to the interchanging pair have been neglected as a further approximation. Our numerical simulation indicates this additional approximation does not significantly affect the kinetics of ordering and phase separation.

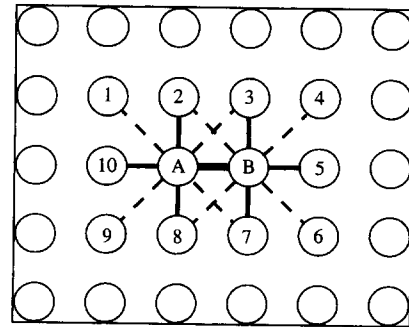


Fig. 2. Schematic illustration of the exchanging pair (A–B) and the influencing lattice sets (1–10) around the pair.

2.4. Rate constant

The reaction rate constant in Eqs. (2) and (3) is calculated according to [13,14]

$$R_{AB}(\{X\}) = \nu \exp \left\{ -\frac{U + 1/2\Delta E}{k_B T} \right\}, \quad (5)$$

where U is the average activation energy for AB exchange, ν is the vibrational frequency associated with the AB exchange, and ΔE is the energy differences before and after an atom exchange and schematically shown in Fig. 3. Since $\nu \exp(-U/k_B T)$ occurs in all configurations, it can be combined with the time, t , in the kinetic equations to give a dimensionless time, t^* ,

$$t^* = t\nu \exp(-U/k_B T). \quad (6)$$

2.5. Numerical solutions to the kinetic equations

In order to solve the kinetic equations numerically, first one needs to construct a supercell containing a certain number of lattice sites. Then initial values for the point and pair distribution functions are assigned at each lattice site. For example, for a completely homogeneous disordered state quenched from an infinite temperature, one may set

$$P_A(\mathbf{r}) = C_A + \zeta(\mathbf{r}), \quad (7)$$

$$P_{AA}(\mathbf{r}_1, \mathbf{r}_2) = P_A(\mathbf{r}_1)P_A(\mathbf{r}_2), \quad (8)$$

where $\zeta(\mathbf{r})$ are small random perturbations to the average composition C_A at lattice site \mathbf{r} . All other points and pair distribution functions are obtained

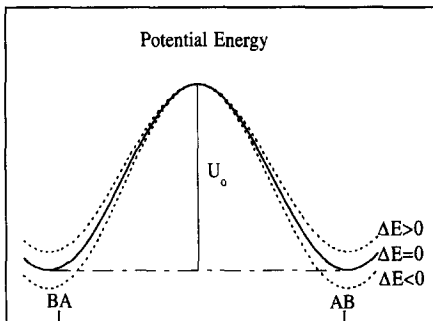


Fig. 3. Illustration of the activation energy for the A–B exchanging process.

from the normalization conditions given in Eq. (1). Based on the initial values for the point and pair distribution functions as well as the A–A, B–B and A–B bond energies and temperature, the rates of change for the point and pair variables are calculated according to the right-hand sides of the kinetic Eqs. (2) and (3). Finally, the equations are integrated using, e.g., the explicit Euler’s method,

$$P_A(\mathbf{r}; t + \Delta t) = P_A(\mathbf{r}; t) + \frac{dP_A(\mathbf{r}; t)}{dt} \Delta t, \quad (9)$$

$$P_{AA}(\mathbf{r}_1, \mathbf{r}_2; t + \Delta t) = P_{AA}(\mathbf{r}_1, \mathbf{r}_2; t) + \frac{dP_{AA}(\mathbf{r}_1, \mathbf{r}_2; t)}{dt} \Delta t,$$

where Δt is the time step for integration. All the information about ordering and phase separation such as local composition, local long-range order, short-range order, antiphase domain or composition domain size can be obtained from the spatial point and pair distribution functions at a given time t .

3. Results and discussions

3.1. The model system

We work with a two-dimensional square lattice with two free surfaces. Periodic boundary conditions are applied parallel to the surface. The direction normal to the surface is treated as a simple termination of the bulk. For example, the A–B pair interchange in Fig. 4a is influenced by only five nearest-neighbor and six second-nearest-neighbor bonds and the A–B pair interchange in Fig. 4b is influenced by four first-nearest-neighbor and four second-nearest-neighbor bonds, as compared to

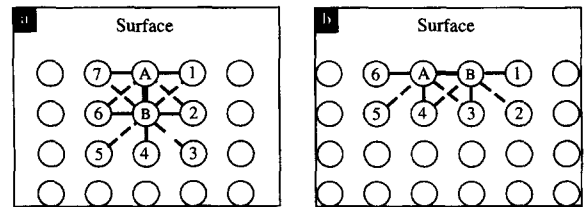


Fig. 4. Schematic illustration of the effect of a surface on the exchanging pair (A–B). (a) The exchange pair normal to the surface; (b) the exchange pair parallel to the surface.

Fig. 2 which shows that an A–B pair interchange in the bulk is affected by six first-nearest-neighbor and eight second-nearest-neighbor bonds. Otherwise, the kinetic equations describing the diffusional process in the surface region are exactly the same as those describing the bulk. The bond energies are chosen to be

$$\begin{aligned} V_{AA}^1 &= 0, & V_{BB}^1 &= 0, & V_{AB}^1 &= 0.3, \\ V_{AA}^2 &= 0, & V_{BB}^2 &= 0, & V_{AB}^2 &= 0.2, \end{aligned}$$

where the superscripts 1 and 2 denote first- and second-neighbor interactions. Therefore, the effective interaction energies are given by

$$\begin{aligned} \varepsilon_1 &= V_{AA}^1 + V_{BB}^1 - 2V_{AB}^1 = -0.6, \\ \varepsilon_2 &= V_{AA}^2 + V_{BB}^2 - 2V_{AB}^2 = -0.4. \end{aligned}$$

The use of a second-neighbor interaction model reduces the interfacial energy anisotropy compared to a first-neighbor interaction model.

The bulk phase diagram and spinodal curves in both the point and pair approximations and for the second-neighbor interaction model are shown in Fig. 5. The phase boundary and spinodal curve for the square lattice in the pair approximation is calculated from the following free energy function:

$$\begin{aligned} F &= 2 \sum_{ij} V_{ij}^1 P_{ij}^1 + 2 \sum_{ij} V_{ij}^2 P_{ij}^2 + k_B T \\ &\times \left(2 \sum_{ij} P_{ij}^1 \ln(P_{ij}^1) + 2 \sum_{ij} P_{ij}^2 \ln(P_{ij}^2) \right. \\ &\left. - 7 \sum_i P_i \ln(P_i) \right), \end{aligned} \quad (10)$$

where i and j represent A or B atoms, P_i , P_{ij}^1 , P_{ij}^2 are point, first-neighbor pair and second-neighbor pair distribution functions, respectively. As discussed earlier, we can choose P_A , P_{AA}^1 , and P_{AA}^2 as independent variables and all other distribution functions can be derived from them. Then, by minimizing the free energy, F , with respect to P_{AA}^1 and P_{AA}^2 , we can express P_{AA}^1 and P_{AA}^2 as a function of P_A . For a system with phase separation, P_A can be replaced by the mole fraction of A, c_A . Therefore, the phase boundary and spinodal curve can be

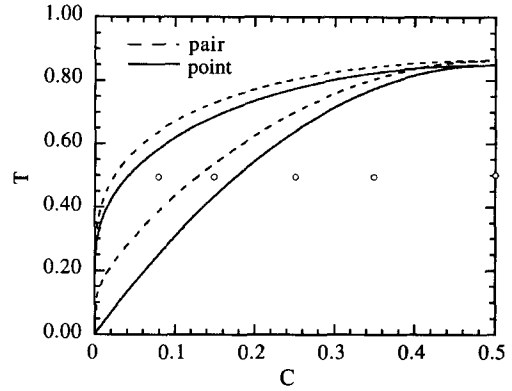


Fig. 5. The bulk phase diagram and spinodal curves in the point and pair approximations with a second-neighbor interaction model.

calculated from the following two conditions,

$$\left(\frac{\partial F}{\partial c_A} \right)_{c_\alpha} = \left(\frac{\partial F}{\partial c_A} \right)_{c_\beta} = \mu_A - \mu_B, \quad \frac{\partial^2 F}{\partial c_A^2} = 0,$$

where μ_A and μ_B are equilibrium chemical potentials for components A and B within the two-phase field at a given temperature, c_α and c_β are two equilibrium compositions at the phase boundary (in the examples discussed in this paper, $c_\beta = 1 - c_\alpha$).

The calculation of phase boundary and spinodal curves in the single-site point approximation is less obvious since the equilibrium state derived from the kinetic Eq. (2) in the point approximation is different from those derived from the traditional Bragg–William mean-field free energy model,

$$\begin{aligned} F &= \frac{1}{2} [z_1 \varepsilon_1 + z_2 \varepsilon_2] c_A^2 \\ &+ k_B T [c_A \ln(c_A) + (1 - c_A) \ln(1 - c_A)], \end{aligned} \quad (11)$$

where z_1 and z_2 are the number of nearest- and second-nearest neighbors. However, according to Refs. [13] and [18], the equilibrium states derived from Eq. (2) can be quite well approximated by the following free energy expression:

$$\begin{aligned} F &= \frac{1}{2} [(z_1 - 1) \varepsilon_1 + z_2 \varepsilon_2] c_A^2 \\ &+ k_B T [c_A \ln(c_A) + (1 - c_A) \ln(1 - c_A)]. \end{aligned} \quad (12)$$

Therefore, the phase boundary and spinodal curves for the point approximation in Fig. 5 are calculated using expression (12).

In the following, simulation results on phase separation near a surface are described for both the point and pair approximations. The compositions studied in this paper are shown in Fig. 5 with small circles. The temporal evolution of morphologies is described by the time-dependent single-site probability function $P_A(r,t)$, which is equivalent to the local composition in systems exhibiting phase separation.

3.2. Off-critical compositions

The temporal morphological evolutions for composition $c = 0.08, 0.15, 0.25$ and 0.35 in the point approximation are shown in Figs. 6–9, respectively.

A common feature to all compositions is that the initial stage involves segregation of solute atoms into the surface region, which results in the development of a concentration wave perpendicular to the surface. This concentration wave gradually propagates into the bulk as the annealing time increases. As an illustration, the average composition in a given layer parallel to the surface is plotted as a function of layer position in Fig. 10 for the alloy with composition 0.35 . In order to see more clearly the development and proration of the concentration wave, the composition profiles at different time steps were shifted with respect to each other. The time step for each composition profile is labeled near a given curve. It appears that a dominant composition wave perpendicular

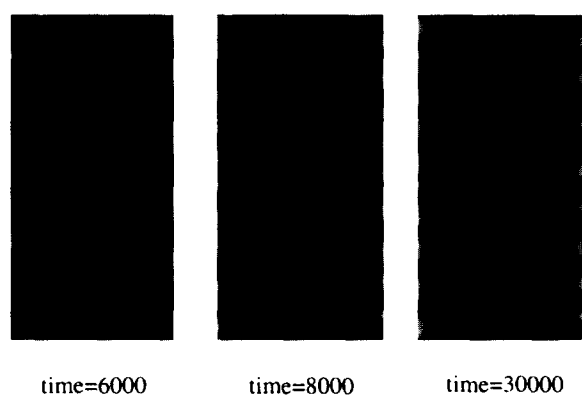


Fig. 6. Morphological pattern formation during surface segregation and spinodal decomposition in an alloy with composition 0.08 and with 128×64 unit cells in the point approximation.

to the surface is present during spinodal decomposition, irrespective of whether or not a material is crystalline or liquid such as polymer melt [2]. It should be emphasized that, in general, a direct comparison between spinodal decomposition near a crystalline surface and that near a liquid surface may be misleading since the hydrodynamic mode may have a very important effect on spinodal morphology and rate of domain coarsening in a liquid, as shown in Ref. [12], whereas in crystalline materials atomic diffusion only takes place among crystal lattice sites, and the interfacial energy anisotropy or the elastic strain may dominate the spinodal morphology [19].

It is interesting to notice that for all compositions it is always the solute atoms which segregate to the surface or to the near-surface region during the initial stage of spinodal decomposition. This is true for both the first- and second-neighbor interaction models. However, the solute-rich layer may disappear during coarsening. For example, for composition $c = 0.35$, the surface layer is initially enriched with solute atoms, but later is depleted during coarsening (Fig. 11).

As shown in Figs. 6–9, the morphologies of spinodal decomposition for the three different compositions are quite different. For composition 0.08 , it is actually outside the spinodal region in the bulk phase diagram for both the point and pair approximations. However, as the composition near the surface increases during segregation, the surface region eventually becomes unstable with respect to spinodal decomposition. Therefore, the particles in the surface layer are a result of pure surface spinodal decomposition. Such surface phase transitions have been observed experimentally [20] and predicted using microscopic theories [21] and Monte Carlo simulations [22] even in systems that the bulk composition is outside the miscibility gap. For compositions 0.15 and 0.25 , initial segregation and the sequential appearance of rows of precipitate particles parallel to the surface result in the formation of distorted hexagonal precipitate lattices. Prolonged coarsening destroyed the regular alignment of precipitate particles. Finally, for composition 0.35 initial spinodal decomposition results in long stripes parallel to the surface near the surface region, whereas in the center region,

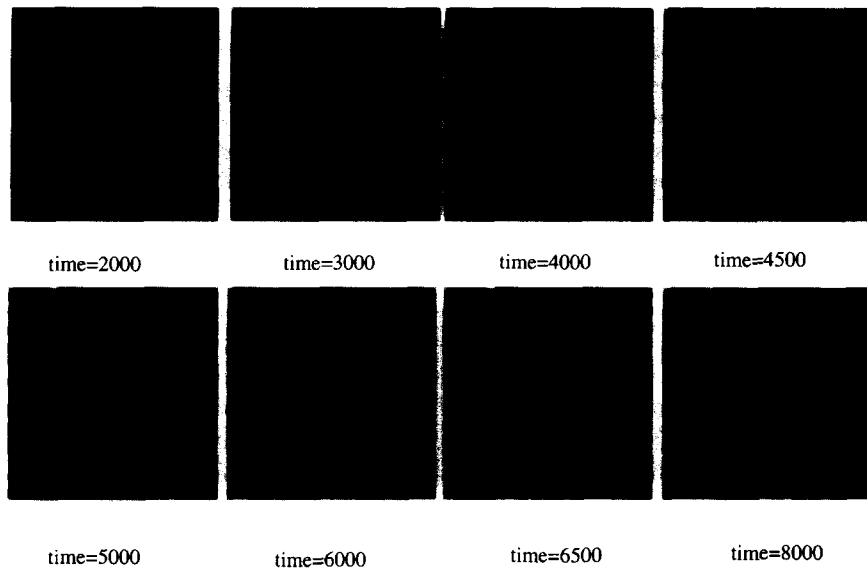


Fig. 7. Morphological pattern formation during surface segregation and spinodal decomposition in an alloy with composition 0.15 and with 128×128 unit cells in the point approximation.

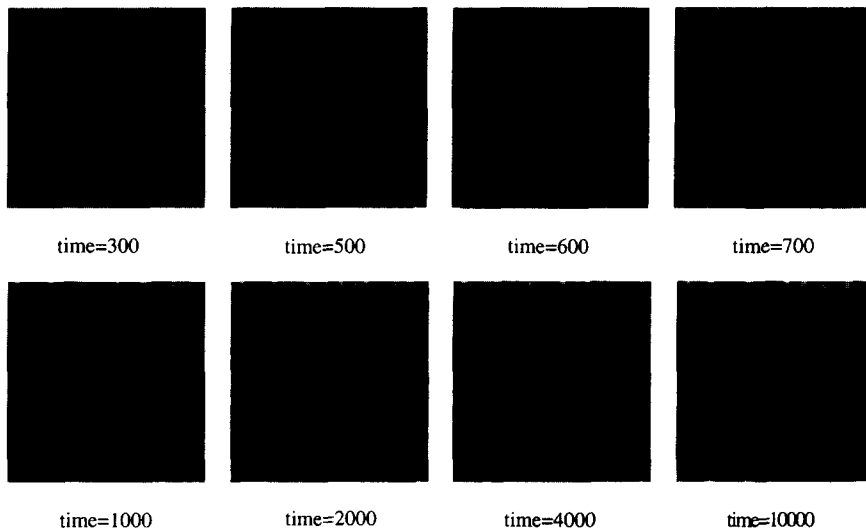


Fig. 8. Morphological pattern formation during surface segregation and spinodal decomposition of an alloy with composition 0.25 and with 128×128 unit cells in the point approximation.

the morphology is similar to that observed in the bulk. Most of the stripes eventually break into particles after long coarsening. One may also notice that the time to develop a two-phase morphology decreases as the composition increases, a result of the increasing driving force for decomposition.

3.3. Critical composition

The morphological evolution for the critical composition $c = 0.5$ is shown in Fig. 12. In Fig. 12, the A–A and B–B bond energies are the same, i.e., $V_{AA}^1 = V_{BB}^1$, $V_{AA}^2 = V_{BB}^2$. No dominant composition

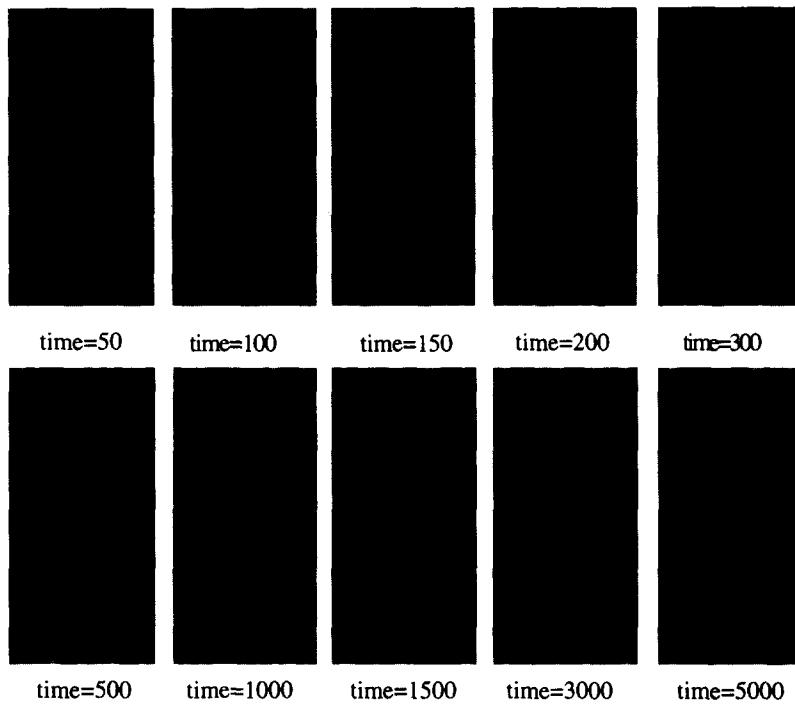


Fig. 9. Morphological pattern formation during surface segregation and spinodal decomposition of an alloy with composition 0.35 and with 128×64 unit cells in the point approximation.

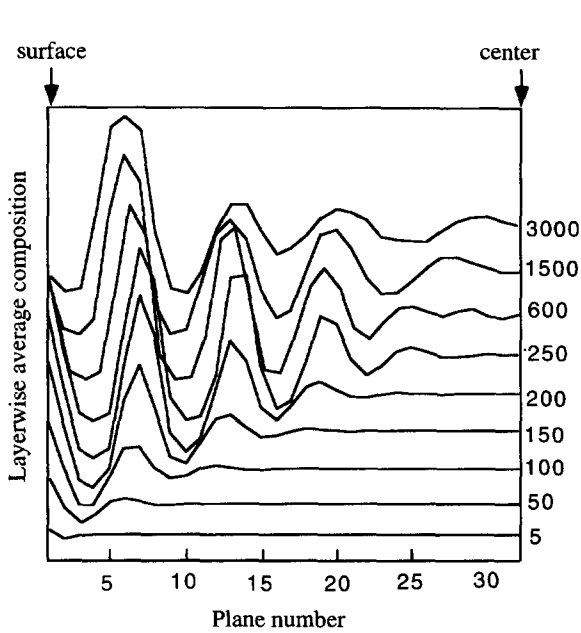


Fig. 10. The average composition in a given layer parallel to the surface plotted as a function of layer number at different simulation times for the alloy with composition 0.35.

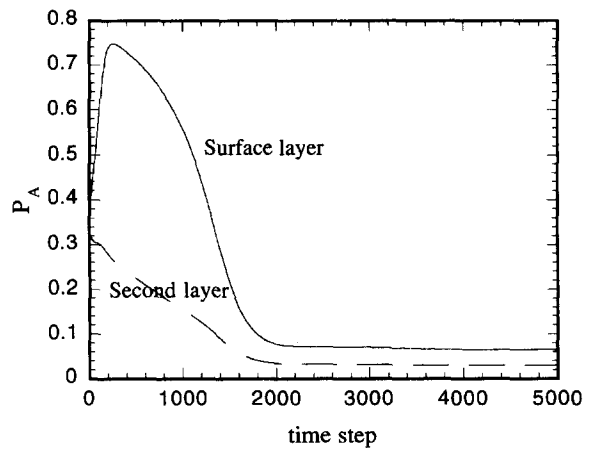


Fig. 11. The temporal changes of the average composition on the first and second layer near the surface for the alloy with composition 0.35.

wave developed parallel to the surface (compared to off-critical compositions discussed above for which a dominant composition wave developed even although the A–A and B–B bond energies are

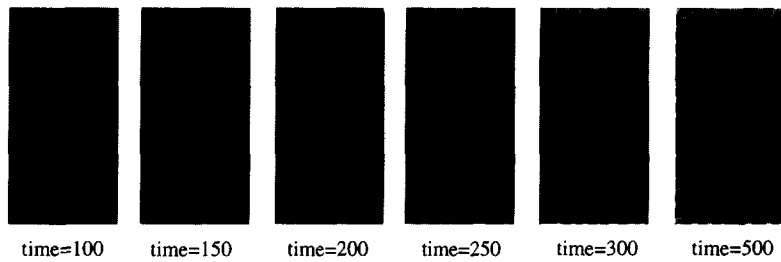


Fig. 12. Morphological pattern formation during surface segregation and spinodal decomposition of an alloy with composition 0.5 in the point approximation. 128×64 unit cells and the A–A and B–B bond energies are the same.

the same). Morphologically there are no stripes near the surface region during the spinodal decomposition and they are very similar to bulk spinodal decomposition at the critical composition. This is easily understandable: as both the composition and the bond energies are the same for A and B atoms, there is no preference for either A or B atoms to occupy the surface region. However, when the A–A and B–B bond energies are different, a dominant spinodal wave developed parallel to the surface, resulting in long stripes near the surface region (Fig. 13).

3.4. Effect of pair correlations

The morphological evolution during spinodal decomposition in the pair approximation is shown in Fig. 14 for composition $c = 0.25$. By comparing Fig. 8 and Fig. 14, one may notice remarkable similarities between morphologies obtained from the point and pair approximations. However, there are two significant differences between the point and pair approximations. First, the incubation time for the pair approximation is at least an order of

magnitude longer than that for the point approximation; the incubation time is defined as the duration of time before any significant composition decomposition takes place. Second, the morphological scale in the pair approximation is much coarser than that in the point approximation if we compare them right after decomposition before any significant coarsening takes place. The main reason for these differences is related to the relaxation kinetics of pair correlations. As one of the authors has shown [23], in bulk systems the relaxation of pair correlations is extremely fast compared to long-range order kinetics and spinodal decomposition kinetics. The relaxation of pair correlations (short-range order) results in a significant decrease in the total free energy (more than half the total free energy decrease from the initially single-phase state to the two-phase decomposed state). As a result, the driving force for the development of composition modulation is significantly reduced, resulting in a much longer incubation time in the pair approximation and a much coarser scale in the decomposed microstructures before any significant coarsening occurs.

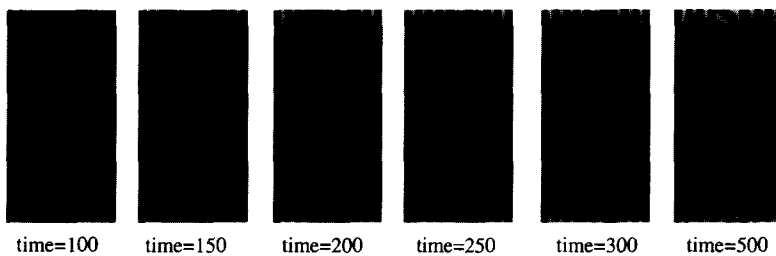


Fig. 13. Morphological evolution for an alloy with composition 0.5 in the point approximation. 128×64 unit cells and the A–A and B–B bond energies are different.

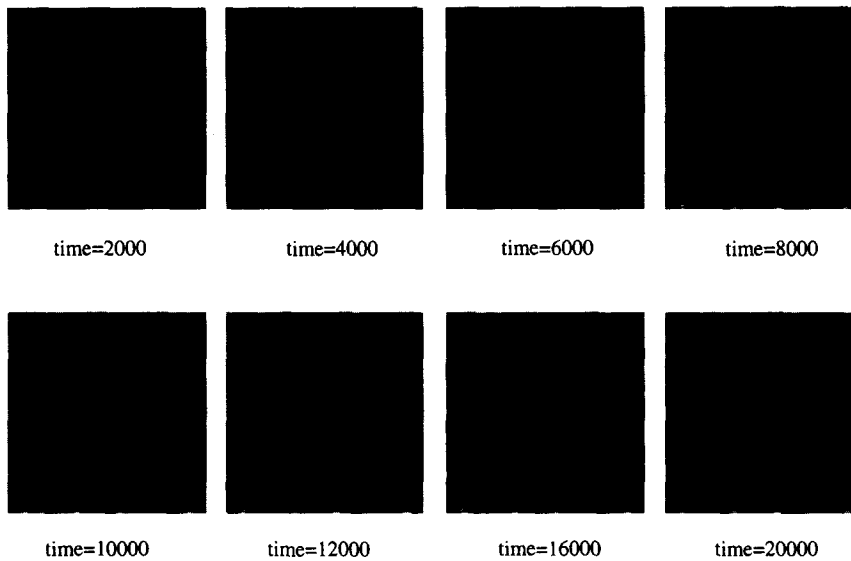


Fig. 14. Morphological evolution during surface spinodal decomposition for an alloy with composition 0.25 and with 128×128 unit cells in the pair approximation.

4. Conclusion

A microscopic kinetic model is developed for studying diffusional processes such as kinetics of surface segregation, segregation profiles, segregation-induced surface phase transformations, ordering and spinodal decomposition near a surface. The kinetics of spinodal decomposition and morphological evolution near a surface were investigated in both the point and pair approximations. It is shown that the initial stage of spinodal decomposition during aging of a single homogeneous phase within a two-phase miscibility gap is surface segregation. As a result, phase decomposition near the surface region develops much earlier than that in the corresponding bulk. It is demonstrated that the presence of a surface leads to the development of a concentration wave with the wave vector normal to the surface. This wave gradually propagates into the bulk, resulting in very interesting morphological patterns such as straight stripes parallel to the surface and precipitation lattices. Most of the straight stripes and precipitation lattices are destroyed during coarsening. It is also shown that the relaxation of pair correlations significantly delayed the development of spinodal

decomposition as compared to that in the point approximation.

Acknowledgements

This work is partially supported by the Petroleum Research Fund, administrated by the American Chemical Society and by NSF under Grant number DMR-9311898. The computer simulations were carried out at the Pittsburgh Supercomputing Center.

References

- [1] R. Kikuchi and L.Q. Chen, *Nanostruct. Mater.* 5 (1995) 257.
- [2] R.A.L. Jones, L.J. Norton, E.J. Kramer, F.S. Bates and P. Wiltzius, *Phys. Rev. Lett.* 66 (1991) 1326; E. Kim, G. Krausch, E.J. Kramer and J.O. Osby, *Macromolecules* 27 (1994) 5927; F. Bruder and R. Brenn, *Phys. Rev. Lett.* 69 (1992) 624; G. Krausch, C.-A. Dai, E.J. Kramer and F.S. Bates, *Phys. Rev. Lett.* 71 (1993) 3669.
- [3] R. Lipowsky, *Phys. Rev. Lett.* 49 (1982) 1575; R. Lipowsky and W. Speth, *Phys. Rev. B* 28 (1983) 3983;

- R. Lipowsky and G. Gompper, *Phys. Rev. B* 29 (1984) 5213.
- [4] K. Binder and D.P. Landau, *Phys. Rev. Lett.* 52 (1984) 318;
D.P. Landau and K. Binder, *Phys. Rev. B* 41 (1990) 4633;
W. Schweika, K. Binder and D.P. Landau, *Phys. Rev. Lett.* 65 (1990) 3321.
- [5] J.M. Sanchez and J.L. Moran-Lopez, *Phys. Rev. Lett.* 58 (1987) 1120; *Phys. Rev. B* 32 (1985) 3534.
- [6] S.M. Foiles, in: *Surface Segregation Phenomena*, Eds. P.A. Dowben and A. Miller (CRC Press, Boca Raton, FL, 1990) pp. 79–106.
- [7] Y. Teraoka and T. Seto, *Surf. Sci.* 255 (1991) 209.
- [8] C. Cserhati, H. Bakker and D.L. Beke, *Surf. Sci.* 290 (1993) 345.
- [9] C. Ball and R.L.H. Essery, *J. Phys.: Condens. Matter* 2 (1990) 10303.
- [10] G. Brown and A. Chakrabarti, *Phys. Rev. A* 46 (1992) 4829.
- [11] S. Puri and K. Binder, *J. Stat. Phys.* 77 (1994) 145.
- [12] F. Krausch, E.J. Kramer, F.S. Bates, J.F. Markov, G. Brown and A. Chakrabarti, *Macromolecules* 27 (1994) 6768.
- [13] L.Q. Chen and J.A. Simmons, *Acta Metall. Mater.* 42 (1994) 2943.
- [14] G.H. Vineyard, *Phys. Rev.* 102 (1956) 981.
- [15] J.W. Cahn, *Acta Metall.* 9 (1961) 795.
- [16] R. Kikuchi, *Phys. Rev.* 81 (1951) 988.
- [17] L.Q. Chen, *MRS Symposium Proceedings* 319 (1994) 375;
C.W. Geng and L.Q. Chen, *Scr. Metall. Mater.* 31 (1994) 1507.
- [18] L.Q. Chen, *Phys. Rev. B* 49 (1994) 3791.
- [19] Y.Z. Wang, L.Q. Chen and A.G. Khachatryan, *Acta Metall. Mater.* 41 (1992) 279, and references therein.
- [20] Y. Liu and P. Wynblatt, *Surf. Sci.* 310 (1994) 27;
W.C. Cheng and P. Wynblatt, *Surf. Sci.* 302 (1994) 302.
- [21] C.R. Helms, *Surf. Sci.* 69 (1977) 689.
- [22] Y. Liu and P. Wynblatt, *Surf. Sci.* 240 (1990) 245.
- [23] L.Q. Chen and J.A. Simmons, unpublished results.